Frequency Domain Analysis and Joint Torque Vibration Suppression Control on Two-Input-Two-Output Torque Difference Amplification Motor Drive System of Electrified Vehicles

Abstract

To improve the cornering performance, a torque vectoring differential (TVD) that generates a torque difference between the left and right wheels has been developed. Particularly, the use of multiple electric traction motors can easily achieve this. A TVD with a two-motor-torque difference amplification mechanism (TDA-TVD), which employs a unique alignment of planetary gears, has been studied and it can generate a larger torque difference compared to an Individual-wheel-drive (IWD) system in the case of using the equal torque output from the traction motors. However, due to the mechanically complicated driving force transmission system including driveshafts and planetary gears, TDA-TVD is prone to cause torsional vibrations of the driveshaft and the yaw rate of the vehicle body while differential torque is generated. A previous study derived a dynamic model TDA-TVD and designed a vibration suppression feedforward controller. While the study demonstrated a certain vibration suppression performance, it did not strictly consider the load side characteristics during the yaw motion. In addition, there was no frequency domain analysis either. On the other hand, this study will analyze TDA-TVD in frequency domain and propose a novel modeling method to construct vibration suppression controllers that deal with both longitudinal motion and yaw motion simultaneously. First, this paper shows a theoretical frequency domain analysis using matrices and obtains resonance frequencies of TDA-TVD. Second, TDA-TVD is modeled based on a summation-differential mode transformation. Third, simulations and experimental evaluations of vibration suppression controls using a real vehicle equipped with the TDA-TVD are demonstrated.

Keywords: Electrified Vehicles, Vibration Suppression Control, Two-Input-Two-Output Torque Difference Amplification Motor Drive System, Frequency Domain Analysis, Torque Vectoring Differential.

Introduction

Actively controlling the yaw rate of the vehicle body is an effective way to enhance the cornering performance. To do this, a torque difference between the left and right wheels must be generated and torque vectoring differential (TVD) has been developed [1-3]. For conventional vehicles with internal combustion engine, torque vectoring was achieved by mainly employing mechanical clutches [3-4] and frictional brakes [5].

On the other hand, some electric vehicles (EVs) employ distributed electric motors as individual-wheel-drive (IWD) systems. Such EVs are actively studied in terms of vehicle dynamics control [6]. A lot of studies proposed torque vectoring or distribution algorithms specially for the such IWD systems [7-15]. The studies [9-13] mainly focused on the stability control of the vehicle maneuver by adjusting torque distribution of in-wheel-motors (IWMs). On the other hand, the studies [16-19] worked on traction control algorithms with different objects or approaches. Integration of vehicle dynamic controls with different

actuators can be seen on [20-22]. Model predictive control has been widely studies thanks to its advantage of online input optimization [23-24]. Vehicle stability control considering autonomous drive are also a trend [25-26]. However, these IWD systems have a fundamental disadvantage of the reduction of the available maximum torque difference and direct yaw moment when the vehicle is cruising at high speed because of the decrease of the maximum motor torque, and when the vehicle is turning with large lateral acceleration due to the load transfer that causes that the inner wheels have less traction force.

In order to increase the available torque difference of electric vehicles, a TVD with a two-motor-torque difference amplification mechanism (TDA-TVD) has been proposed by a group of Sawase [27-28]. Two traction motors are used for TDA-TVD to drive rear two wheels. The unique feature of TDA-TVD is that the left and right sides are mechanically coupled as seen in Figure 1, making it considered as the two-input-two-output drive system. TDA-TVD further amplifies differential torque inputs compared to the conventional IWD system (either onboard motors (OMBs) or IWMs) with the same electric traction motor, and it was suggested that the cornering performance could be improved [27-28]. The use of TDA-TVD will have economic benefits to achieve larger maximum torque difference. Without TDA-TVD, larger maximum torque difference could only achieved by increasing the motor size, which results in higher costs (for both MOBs or IWMs). However, TDA-TVD also increases vibrations of the driveshaft torque on the wheels and consequential yaw rate vibration of the vehicle body during cornering because of the amplified differential torque.

The driveline of vehicles including internal combustion engines, transmissions, driveshafts, and tires can be the source of vibration. In the case of EVs, relatively fast torque response of electric motors can cause torsional vibration of the driveline such as driveshafts. To deal with this potential issue, some studies designed anti-vibration controllers [29-37]. Most of them targeted EVs with drive systems which drives two of front or rear wheels with a single motor, or the left and right wheels individually with two motors. Therefore, those conventional methods cannot be effectively applied to TDA-TVD because of its fundamentally different mechanical structure.

To deal with this issue, a previous study derived a linearized model of TDA-TVD and designed a vibration suppression feedforward controller [38]. The derived linearized model assumed a constant load model (when vehicle is going on straight paths), which does not guarantee its performance for any situations (e.g., cornering). Furthermore, the parameter tuning of the vibration suppression controller was based on time-domain analysis (i.e., waveform of measured driveshaft torque), which could be time-consuming.

This study provides improved methods to construct controllers for TDA-TVD. This study first analyzes TDA-TVD in the frequency domain in detail, clarifying resonance frequencies and corresponding vibration modes. Second, this study proposes a novel linearized model of TDA-TVD that well describes the longitudinal motion and yaw

motion using a coordinate transformation. By doing this, a frequency domain analysis of the real hardware of TDA-TVD will be much easier. Furthermore, the driveshaft torque vibration of the longitudinal and yaw modes could be effectively mitigated by designing controllers for the corresponding modes.
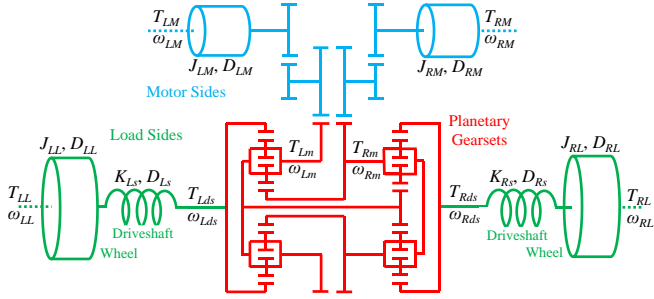

Figure 1. Dynamic model of TDA-TVD.

Dynamic model of TDA-TVD on normal mode

TDA-TVD could be designed in multiple types [27-28]. Figure 1 shows an example of schematic diagram of TDA-TVD. All types of TDA-TVD can be comprehensively represented by a speed diagram as shown in Figure 2 using b_1 and b_2 [28]. In the figure, b_1 and b_2 are the equivalent secondary reduction gear ratios which represent the amplification ratio of the differential torque input ($b_1 \doteqdot b_2$ for practicality).

Derivation of Dynamic Model of TDA-TVD on Normal Mode

In the previous study, vectors and matrices are partly used to derive the dynamic model of TDA-TVD, but in this study, they are fully employed for simpler and more organized representation. Previously, from Figure 1 and 2, a dynamic model of TDA-TVD was derived as shown in Figure 3(a) and Figure 3(b) [38]. In Figure 3(a), motor torque and angular speeds are chosen as inputs and outputs, and the driveshaft side components are converted to the motor side. Conversely, in Figure 3(b), the motor side components are converted to the driveshaft side. The second block diagram is convenient to use for controlling the driveshaft side angular speed $\omega_{R(L)ds}$ and driveshaft torque $T_{R(L)ds}$. In this block diagram, a driveshaft side torque input $T_{R(L)in}$ is converted from the input motor torque $T_{R(L)M}$ as shown in (1), and a driveshaft side angular speed $\omega_{R(L)ds}$ is converted from the motor side angular speed $\omega_{R(L)M}$ as shown in (2). These two equations represent the static relationship between motor side and driveshaft side.

$$T_{in} = BGT_M \tag{1}$$

where $\quad T_{in} \stackrel{\text{def}}{=} \begin{bmatrix} T_{Rin} \\ T_{Lin} \end{bmatrix}, B \stackrel{\text{def}}{=} \begin{bmatrix} b_2+1 & -b_2 \\ -b_1 & b_1+1 \end{bmatrix},$

$$G \stackrel{\text{def}}{=} \begin{bmatrix} G_R & 0 \\ 0 & G_L \end{bmatrix}, T_M \stackrel{\text{def}}{=} \begin{bmatrix} T_{RM} \\ T_{LM} \end{bmatrix}$$

$$\omega_{ds} = B^{-1}G\omega_M \tag{2}$$

where $\quad \omega_{ds} \stackrel{\text{def}}{=} \begin{bmatrix} \omega_{Rds} \\ \omega_{Lds} \end{bmatrix}, \omega_L \stackrel{\text{def}}{=} \begin{bmatrix} \omega_{RM} \\ \omega_{LM} \end{bmatrix}$

The following three equations represent the dynamics of the left and right wheels, motors, and driveshafts.

$$\omega_L = P_L(T_{ds} - T_L) \tag{3}$$

$$\omega_{ds} = B^{-1}G^{-1}P_M G^{-1}(B^T)^{-1}(T_{in} - T_{ds}) \tag{4}$$

$$T_{ds} = P_{ds}(\omega_{ds} - \omega_L) \tag{5}$$

where $\quad \omega_L \stackrel{\text{def}}{=} \begin{bmatrix} \omega_{RL} \\ \omega_{LL} \end{bmatrix}, T_L \stackrel{\text{def}}{=} \begin{bmatrix} T_{RL} \\ T_{LL} \end{bmatrix}, T_{ds} \stackrel{\text{def}}{=} \begin{bmatrix} T_{Rds} \\ T_{Lds} \end{bmatrix},$

$$P_L \stackrel{\text{def}}{=} \begin{bmatrix} 1/(J_{RL}s + D_{RL}) & 0 \\ 0 & 1/(J_{LL}s + D_{LL}) \end{bmatrix},$$

$$P_M \stackrel{\text{def}}{=} \begin{bmatrix} 1/(J_{RM}s + D_{RM}) & 0 \\ 0 & 1/(J_{LM}s + D_{LM}) \end{bmatrix},$$

$$P_{ds} \stackrel{\text{def}}{=} \begin{bmatrix} D_{Rs} + K_{Rs}/s & 0 \\ 0 & D_{Ls} + K_{Ls}/s \end{bmatrix}$$

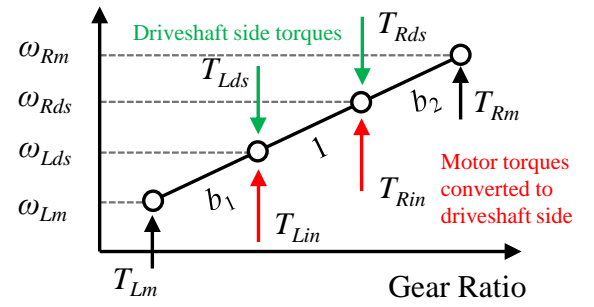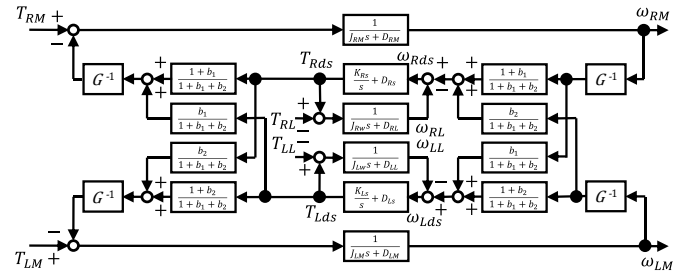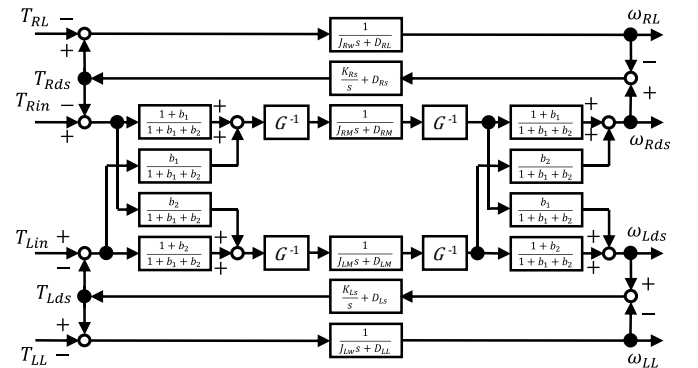where each variable is defined or derived as follows

Figure 2. Speed diagram of TDA-TVD.

(a) Converted to motor side.

(b) Converted to driveshaft side [38].

Figure 3. Block diagrams of linearized normal model of TDA-TVD.

Derivation of Linear Model of TDA-TVD on Normal Mode

The previous study [38] delivered a linearized normal model by assuming $T_{RL} = T_{LL} = 0$ and $J_{RL} = J_{LL} = J_w + r^2 M/2$, i.e., which is in the case the vehicle is proceeding on straight paths and the wheels are not slipping.

Transfer functions of linear model of TDA-TVD could be also represented by matrices effectively. From the equations (3-5), we have the following equation

$$T_{ds} = [B^T G P_M^{-1} G B (P_{ds}^{-1} + P_L) + E_2]^{-1} T_{in}$$

$$= \begin{bmatrix} T_{Rds}/T_{Rin} & T_{Rds}/T_{Lin} \\ T_{Lds}/T_{Rin} & T_{Lds}/T_{Lin} \end{bmatrix} T_{in} = \begin{bmatrix} g_{11} & g_{12} \\ g_{21} & g_{22} \end{bmatrix} T_{in} \quad (6)$$

where E_2 is a 2x2 identity matrix. Each component of the matrix above is the transfer function between $T_{R(L)in}$ and $T_{R(L)ds}$. These matrices representation can handle different left and right side parameters, but for the practicality, they are designed to be as equal as possible.

Now we assume all the left and right side parameters except for b_1 and b_2 are equal (e.g., $G_R = G_L = G$, $K_{Rs} = K_{Ls} = K_s$, etc.). In that case, G, P_{ds}, P_M, and P_L become scalars. The above equation will become

$$T_{ds} = [XZ + E_2]^{-1} T_{in}$$

$$= \frac{X_d}{Y} \begin{bmatrix} Z_{22} X_n + X_d & -X_n Z_{12} \\ -X_n Z_{21} & Z_{11} X_n + X_d \end{bmatrix} T_{in} \quad (7)$$

Where $\qquad Z \stackrel{\text{def}}{=} B^T B$

$$= \begin{bmatrix} (b_2 + 1)^2 + b_1^2 & -b_1^2 - b_1 - b_2^2 - b_2 \\ -b_1^2 - b_1 - b_2^2 - b_2 & (b_1 + 1)^2 + b_2^2 \end{bmatrix} = \begin{bmatrix} Z_{11} & Z_{12} \\ Z_{21} & Z_{22} \end{bmatrix}$$

$$X \stackrel{\text{def}}{=} \frac{X_n}{X_d} = \frac{G^2 (J_M s + D_M)[J_L s^2 + (D_L + D_s)s + K_s]}{(J_L s + D_L)(D_s s + K_s)}$$

$$Y \stackrel{\text{def}}{=} X_n^2 |Z| + X_n X_d (Z_{11} + Z_{22}) + X_d^2$$

$$|Z| = (b_1 + b_2 + 1)^2$$

Since left and right sides of TDA-TVD are 1DOF systems, ω_{Rds}, ω_{RL}, T_{Rds} have one-to-one-one relationships with each other, which is given by the following equations (and also for between ω_{Lds}, ω_{LL}, T_{Lds}),

$$\omega_{ds} = \frac{J_L s^2 + (D_L + D_s)s + K_s}{(J_L s + D_L)(D_s s + K_s)} T_{ds} \quad (8)$$

$$\omega_L = \frac{1}{J_L s + D_L} T_{ds} \quad (9)$$

we can also obtain the transfer functions with the driveshaft-side angular speed or wheel speed being outputs (i.e., from T_{in} to ω_{ds}, or , ω_L). By also using (5) and (6), we can derive other transfer function matrix such as from T_M to ω_M.

Frequency Response Analysis of TDA-TVD on Normal Mode

A frequency domain analysis has numerous advantages in system identification (modeling and parameter fitting), controller design and parameter tuning (securing both performance and stability margin). As we obtained the basic transfer functions of TDA-TVD, we are going

to give the frequency domain analysis of TDA-TVD next. Since the linear model of TDA-TVD is classified as two-degree-of-freedom (2DOF) system, there are two vibration modes and corresponding resonance frequencies ω_{rL} (lower resonance frequency) and ω_{rH} (higher resonance frequency). Those are the roots of the following characteristic equation.

$$Y|_{s = j\omega_{rL(H)}} = 0 \quad (10)$$

Approximated resonance frequencies could be obtained by assuming all the viscosity to be zero (i.e., $D_L = D_s = D_M = 0$).

$$\omega_{rL} = \sqrt{K_s \left[\frac{1}{J_L} + \frac{1}{2|J|} \left(J_X - \sqrt{J_X^2 - 4|J|} \right) \right]},$$

$$\omega_{rH} = \sqrt{K_s \left[\frac{1}{J_L} + \frac{1}{2|J|} \left(J_X + \sqrt{J_X^2 - 4|J|} \right) \right]} \quad (11)$$

where $\qquad J = \begin{bmatrix} J_{11} & J_{12} \\ J_{21} & J_{22} \end{bmatrix} = G^2 J_M Z$

$$J_X = J_{11} + J_{22} = G^2 J_m (b_1^2 + b_2^2 + b_1 + b_2 + 1)$$

If we assume $J_{11} = J_{22}$ (i.e., $b_1 = b_2$ which is a reasonable assumption), these equations will be simplified as

$$\omega_{rL} = \sqrt{K_s \left(\frac{1}{J_L} + \frac{1}{J_{11} - J_{12}} \right)} \approx \sqrt{\frac{K_s}{J_{11} - J_{12}}},$$

$$\omega_{rH} = \sqrt{K_s \left(\frac{1}{J_L} + \frac{1}{J_{11} + J_{12}} \right)} \approx \sqrt{\frac{K_s}{J_{11} + J_{12}}} \quad (12)$$

It should be noted that $J_{12} < 0$, so $\sqrt{K_s/(J_{11} - J_{12})} < \sqrt{K_s/(J_{11} + J_{12})}$ holds. The approximation is reasonable since usually $J_L \gg (J_{11} \mp J_{12})$ satisfies. In other words, the resonance frequencies are virtually determined by the motor inertia.

The left and right side motor inertia vibrate in the same phase (summation mode) at the higher resonance frequency ω_{rH}, and the opposite phase (differential mode) at the lower resonance frequency ω_{rL}, which could be identified by substituting $s = j\omega_{rL(H)}$ and $T_{in} = 0$ to (3-5).

On the other hand, the anti-resonance frequency ω_a can be obtained by finding the root of the numerator of the common term of the transfer function matrix, i.e.,

$$X_d|_{s = j\omega_a} = 0 \quad (13)$$

By solving this equation, we get

$$\omega_a = \sqrt{\frac{K_s}{J_L}} \quad (14)$$

This vibration mode is solely determined by the load side inertia, naturally due to the fact that the motor side does not vibrate at all when anti resonance is occurring.

(a) ω_{LM}/T_{LM}.
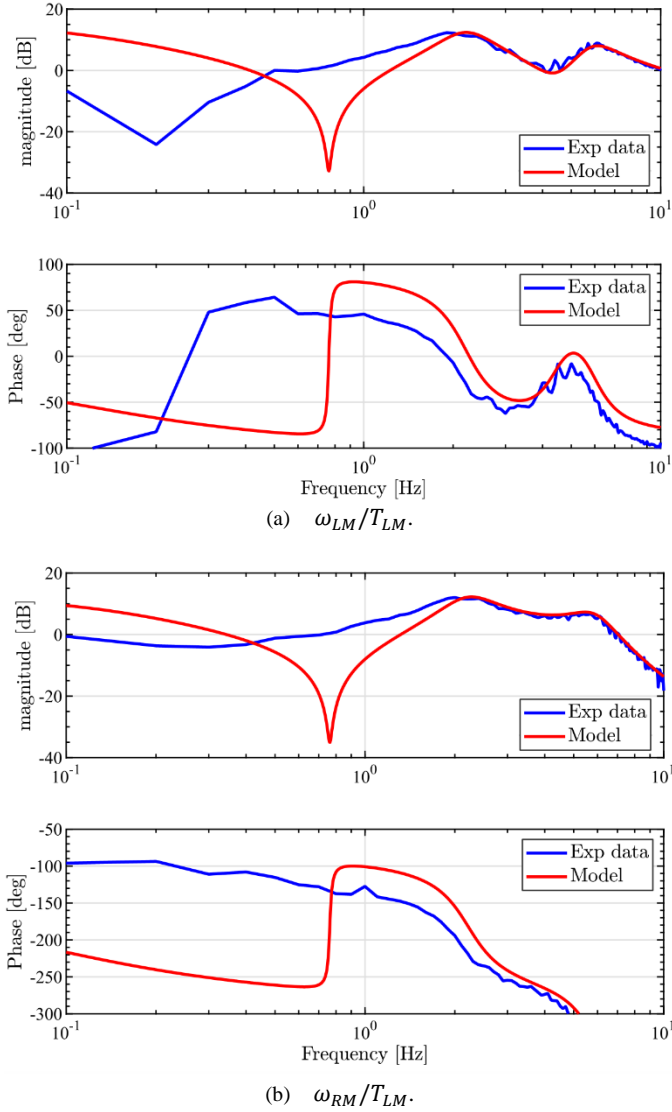

(b) ω_{RM}/T_{LM}.

Figure 4. Frequency responses of TDA-TVD on normal mode in both theoretical fitting model and real hardware bench. While the higher frequency region above 2 Hz has decent agreement between the experimental results and fitting model, lower frequency region has significantly different curves.

Frequency-domain System Identification of TDA-TVD on Normal Mode

The previous study took left and right motor torques $T_{R(L)M}$ (or $T_{R(L)in}$) as inputs and left and right motor wheel speeds $\omega_{R(L)M}$ (or $\omega_{R(L)ds}$) as outputs and assumed the load inertia as $J_{RL} = J_{LL} = J_w + r^2 M/2$ for the linear model of TDA-TVD. This mode has issues with emulating the differential torque inputs and differential rotation, which will be explained in this section.

The frequency response of TDA-TVD on normal mode is obtained by both the theoretical transfer functions and experiments of the system identification using chirp sine wave torque inputs to a real hardware bench with the TDA-TVD unit. Offset torques are also added to eliminate the effect of the backlash of the driven gears. The first order polynomial of the measured angular speeds are removed using "detrend" function of MATLAB. The bench is equipped with two independent electric motors to emulate a load model proceeding on straight path (i.e., left and right wheel speeds are kept equal). The bode diagrams of the frequency responses are shown in Figure 4. These are obtained by using "frd" function of MATLAB. There is a decent

agreement between the fitting model and experimental results at higher frequency (above 2 Hz). However, at lower frequency, there is a significant difference between them. While two resonance frequencies are identifiable, anti-resonance frequency cannot be. This is because the linearized normal model has no restriction of differential rotation but there is the restriction of it on the real bench and real vehicles. Therefore, the load characteristics (e.g., apparent nominal inertia) changes in the real vehicles, while the linearized normal model assumes constant load. Overall, this clearly shows the limitation of the linear model with normal mode. The agreement on the higher frequency suggests that the derived model of TDA-TVD is reliable, except for loads (wheels). This is the major motivation why we would like to propose the next approach.

Dynamic model of TDA-TVD with summation-differential mode transformation

The previous approach requires the decoupling compensator. Not only it makes the overall controller architecture more complex, but also the linearized model does not effectively consider the yaw motion, which varies the apparent load inertia. Since the behavior of the vehicle is drastically different in both cases, it is better to construct the dynamic model of each state respectively and their corresponding controllers. We define a summation mode in which the vehicle is translating, and a differential mode in which the vehicle is rotating in the yaw axis. The idea of coordinate transformation can be seen on [39-40], where mathematical operation makes it easier to handle seemingly complex plants.

Derivation of Dynamic Model of TDA-TVD with summation-differential mode transformation

(4) can be simplified by assuming the left and right side parameters are equal to each other (except for $b_1 \neq b_2$) as follows

$$\boldsymbol{\omega}_{ds} = G^{-2} P_M \boldsymbol{Z}^{-1} (\boldsymbol{T}_{in} + \boldsymbol{T}_{ds}) \tag{15}$$

From the above equation, it is clear that the both input torques T_{Rin} and T_{Lin} affect to the output angular speed ω_{Lds} and ω_{Rds}, since the matrix $\boldsymbol{Z}^{-1}$ is not diagonal, which is also visible in the coupling blocks in the block diagrams of TDA-TVD. If we could make this matrix diagonal by certain proper coordinate transformation, we can decouple the model into two of 1DOF systems.

Fundamentally, TDA-TVD is a device that further amplifies differential torque inputs. Therefore, it is natural to decouple the systems in two modes; summation and differential modes, where equal and differential input torques are applied to the left and right side wheels. In order to convert a dynamic model of TDA-TVD by summation-differential mode transformation (SDMT), we need to multiply a coordinate transformation matrix $\boldsymbol{A}$ to each of input and output parameters, which is given by

$$A = \frac{1}{2}\begin{bmatrix} 1 & 1 \\ 1 & -1 \end{bmatrix} \tag{16}$$

Load side dynamics are easy to perform the SDMT because there is no couplings between left and right systems. The dynamics of the load and the driveshaft can be represented in summation and differential modes, which is given by

$$A\boldsymbol{\omega}_L = AP_L(\boldsymbol{T}_{ds} - \boldsymbol{T}_L) \tag{17}$$

$$\begin{bmatrix} \dfrac{1}{2} & \dfrac{1}{2} \\ \dfrac{1}{2} & -\dfrac{1}{2} \end{bmatrix} \begin{bmatrix} \omega_{RL} \\ \omega_{LL} \end{bmatrix} = P_L \begin{bmatrix} \dfrac{1}{2} & \dfrac{1}{2} \\ \dfrac{1}{2} & -\dfrac{1}{2} \end{bmatrix} \begin{bmatrix} T_{Rds} - T_{RL} \\ T_{Lds} - T_{LL} \end{bmatrix}$$

$$= \begin{bmatrix} \omega_{SL} \\ \omega_{DL} \end{bmatrix} = P_L \begin{bmatrix} T_{Sds} - T_{SL} \\ T_{Dds} - T_{DL} \end{bmatrix}$$

$$\boldsymbol{A}\boldsymbol{T}_{ds} = \boldsymbol{A}P_{DS}(\boldsymbol{\omega}_{ds} - \boldsymbol{\omega}_L)$$

$$\begin{bmatrix} \dfrac{1}{2} & \dfrac{1}{2} \\ \dfrac{1}{2} & -\dfrac{1}{2} \end{bmatrix} \begin{bmatrix} T_{Rds} \\ T_{Lds} \end{bmatrix} = P_{DS} \begin{bmatrix} \dfrac{1}{2} & \dfrac{1}{2} \\ \dfrac{1}{2} & -\dfrac{1}{2} \end{bmatrix} \begin{bmatrix} \omega_{Rds} - \omega_{RL} \\ \omega_{Lds} - \omega_{LL} \end{bmatrix} \qquad (18)$$

$$= \begin{bmatrix} T_{Sds} \\ T_{Dds} \end{bmatrix} = P_{DS} \begin{bmatrix} \omega_{Sds} - \omega_{SL} \\ \omega_{Dds} - \omega_{DL} \end{bmatrix}$$

where the additional letter of either S or D on the subscript represents summation or differential mode, respectively. Now, we would like to multiply (36) by $\boldsymbol{A}$ and it is given by

$$\boldsymbol{A}\boldsymbol{\omega}_{ds} = \boldsymbol{A}G^{-2}P_M \boldsymbol{Z}^{-1}(\boldsymbol{T}_{in} - \boldsymbol{T}_{ds})$$

$$= G^{-2}P_M \boldsymbol{C}\boldsymbol{A}(\boldsymbol{T}_{in} - \boldsymbol{T}_{ds}) \qquad (19)$$

$$= \begin{bmatrix} \omega_{Sds} \\ \omega_{Dds} \end{bmatrix} = G^{-2}P_M \boldsymbol{C} \begin{bmatrix} T_{Sin} - T_{Sds} \\ T_{Din} - T_{Dds} \end{bmatrix}$$
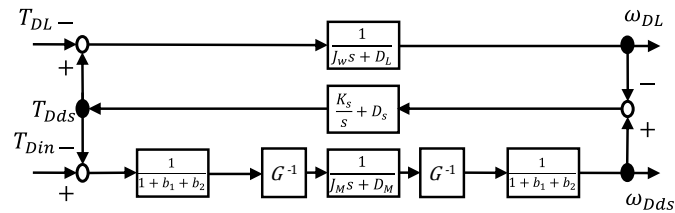
where $\boldsymbol{C}$ is a certain diagonal matrix to obtain. In order to satisfy the above equation, $\boldsymbol{Z}^{-1}$ has to satisfy

$$\boldsymbol{A}\boldsymbol{Z}^{-1} = \boldsymbol{C}\boldsymbol{A} \qquad (20)$$

This condition only satisfies if $b_1 = b_2$ holds. Thankfully, b_1 and b_2 are designed to be close as possible so this condition of the approximation is acceptable. With this approximation $b_1 = b_2 \approx b = (b_1 + b_2)/2$, $\boldsymbol{C}$ is given by
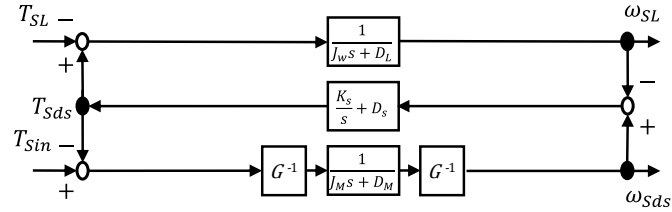
(a) Summation mode.

(b) Differential mode.

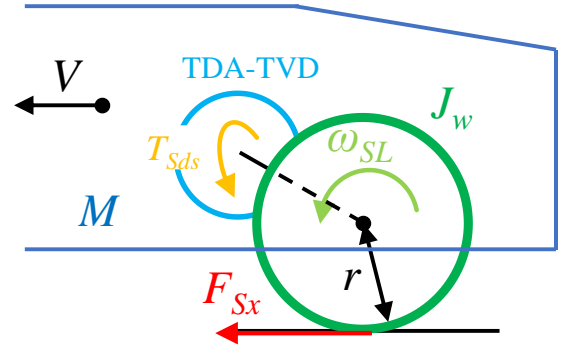Figure 5. Block diagrams of linearized normal model of TDATVD.

Figure 6. Accelerating vehicle.

$$\boldsymbol{C} = \begin{bmatrix} 1 & 0 \\ 0 & \dfrac{1}{|\boldsymbol{Z}|} \end{bmatrix} = \begin{bmatrix} 1 & 0 \\ 0 & \dfrac{1}{(b_1 + b_2 + 1)^2} \end{bmatrix} \qquad (21)$$

The above equation is a diagonal matrix, which indicates that each mode is decoupled from each other. Now we have the block diagram of TDA-TVD in both the summation and differential modes as shown in Figure 5(a) and Figure 5(b). The unique feature of the torque differential amplification only appears on the differential mode, which agrees with the intended function of TDA-TVD.

Derivation of Linear Model of TDA-TVD on Summation Mode

A linearization of the dynamic model of TDA-TVD on summation and differential modes is required to construct controllers. The linearization here means the load torque T_L is solely determined by the input torque T_{in} so that T_L can be replaced by an equivalent load side dynamic. On the summation mode, we consider the vehicle accelerating on straight paths as shown in Figure 6.

We have the following equations to describe the acceleration of the wheels and vehicle
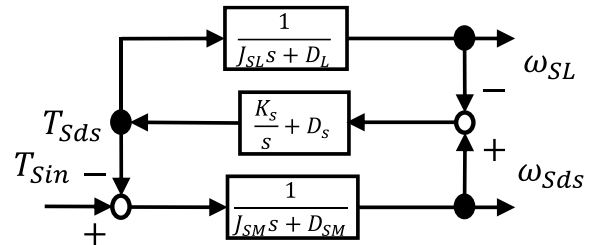

Figure 7. Block diagram of linearized TDA-TVD in summation mode.

$$\omega_{SL} = \frac{1}{J_w s + D_L}(T_{Sds} - T_{SL}) \qquad (22)$$

$$T_{SL} = rF_{Sx} \qquad (23)$$

$$V_x = \frac{2}{Ms}F_{Sx} \qquad (24)$$

$$V_{SL} = r\omega_{SL} \qquad (25)$$

$$\lambda_S = \frac{V_{SL} - V_x}{V_{SL}} \qquad (26)$$

where V_x is the longitudinal vehicle body speed and λ_S is the summation slip ratio. From these equations, we get the transfer function of the linear model as follows

$$\frac{\omega_{SL}}{T_{Sds}} = \frac{1}{[J_w + r^2 M(1 - \lambda_{Sn})/2]s + D_L} = \frac{1}{J_{SL}s + D_L} \quad (27)$$

where J_{SL} and λ_{Sn} are the equivalent load inertia and nominal slip ratio on the summation mode. The block diagram of the linearized model of TDA-TVD on the summation mode is shown in Figure 7. In the figure, the motor inertia and viscosity on the summation mode J_{SM} and D_{SM} are multiplied by G^2 from the original value. Some of transfer functions of this summation mode are given by

$$\frac{T_{Sds}}{T_{Sin}} = \frac{(J_{SL}s + D_L)(D_s s + K_s)}{c_3 s^3 + c_2 s^2 + c_1 s + c_0} \quad (28)$$

where $c_3 = J_{SM}J_{SL}, c_2 = J_{SM}(D_L + D_s) + J_{SL}(D_{SM} + D_s)$

$c_1 = D_{SM}D_L + D_{SM}D_s + D_L D_s + K_s(J_{SM} + J_{SL}), c_0 = (D_{SM} + D_L)K_s$

$$\frac{\omega_{Sds}}{T_{Sin}} = \frac{J_{SL}s^2 + (D_L + D_s)s + K_s}{c_3 s^3 + c_2 s^2 + c_1 s + c_0} \quad (29)$$

$$\frac{\omega_{SL}}{T_{Sin}} = \frac{D_s s + K_s}{c_3 s^3 + c_2 s^2 + c_1 s + c_0} \quad (30)$$

Derivation of Linear Model of TDA-TVD on Differential Mode

On the differential mode, we consider the rotating vehicle as shown in Figure 8. The left and right wheel have the different longitudinal
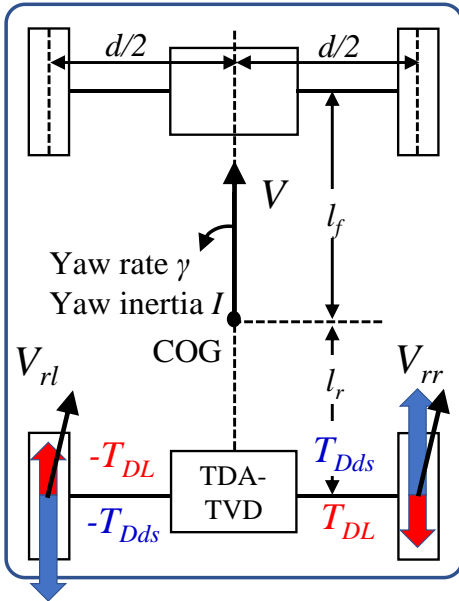

Figure 8. Rotating vehicle.

vehicle speed from the longitudinal vehicle body speed V_x due to the yaw rate γ, which is given by

$$V_{rrx} = V_x + \frac{d}{2}\gamma$$

$$V_{rlx} = V_x - \frac{d}{2}\gamma \quad (31)$$

Therefore, a differential longitudinal vehicle speed between the left and right wheels V_{Dx} is given by

$$V_{Dx} = \frac{V_{rrx} - V_{rlx}}{2} = \frac{d}{2}\gamma \quad (32)$$

With the equation above, we can define the differential slip ratio λ_D as follows

$$\lambda_D = \frac{r\omega_{DL} - V_{Dx}}{r\omega_{DL}} \quad (33)$$

Now, the yaw rate and the differential angular speed ω_{DL} can be related, which is given by

$$\gamma = \frac{r}{d/2}(1 - \lambda_D)\omega_{DL} \quad (34)$$

We have the following equations to describe the yaw rotation of the wheels and vehicle [41]

$$\omega_{DL} = \frac{1}{J_w s + D_L}(T_{Dds} - T_{DL}) \quad (35)$$

$$T_{DL} = rF_{Dx} \quad (36)$$

$$I\dot{\gamma} = -2C_f l_f\left(\beta + \frac{l_f}{V}\gamma - \delta_f\right) + 2C_r l_r\left(\beta - \frac{l_r}{V}\gamma\right) + \frac{d}{2}2F_{Dx} \quad (37)$$
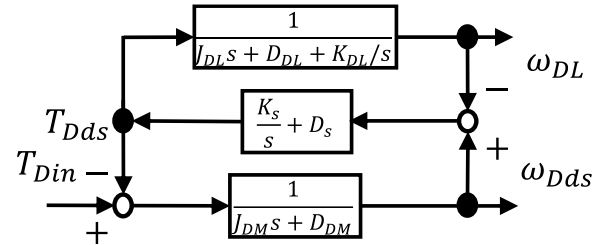
$$a_y = V(\beta s + \gamma) \quad (38)$$

Figure 9. Block diagram of linearized TDA-TVD in differential mode.

Since we only consider yaw motion while on the straight paths, $\delta_f = 0$ and $a_y = 0$ hold. This assumption is also helpful to simplify the model and controller. With these, we can derive the following transfer function

$$\frac{\omega_{DL}}{T_{Dds}} = \frac{s}{J_{DL}s^2 + D_{DL}s + K_{DL}} \quad (39)$$

$$J_{DL} = J_w + \frac{2r^2}{d^2}(1 - \lambda_{Dn})I \quad (40)$$

$$D_{DL} = D_L + \frac{4r^2}{d^2 V}(1 - \lambda_{Dn})(C_f l_f^2 + C_r l_r^2) \quad (41)$$

$$K_{DL} = \frac{4r^2}{d^2}(1 - \lambda_{Dn})(C_r l_r - C_f l_f) \quad (42)$$

where J_{DL}, D_{DL}, K_{DL} and λ_{Dn} are the equivalent load inertia, load damping factor, load elasticity factor, and nominal slip ratio on the differential mode. If the vehicle is neutral steer (NS), then $K_{DL} = 0$

satisfies. The block diagram of the linearized model of TDA-TVD on the differential mode is shown in Figure 9. In the figure, the motor inertia and viscosity on the differential mode J_{DM} and D_{DM} are multiplied by $G^2(1 + b_1 + b_2)^2$ from the original value.

Transfer functions $\frac{T_{Dds}}{T_{Din}}$, $\frac{\omega_{Dds}}{T_{Din}}$, and $\frac{\omega_{SL}}{T_{Sin}}$ of this differential mode of the NS vehicle ($K_{DL} = 0$) can be represented in the same form as (28-30).

$$\frac{T_{Dds}}{T_{Din}} = \frac{(J_{DL}s + D_{DL})(D_s s + K_s)}{d_3 s^3 + d_2 s^2 + d_1 s + d_0} \quad (43)$$

where $d_3 = J_{DM}J_{DL}, d_2 = J_{DM}(D_{DL} + D_s) + J_{DL}(D_{DM} + D_s)$,

$d_1 = D_{DM}D_{DL} + D_{DM}D_s + D_{DL}D_s + K_s(J_{DM} + J_{DL}), d_0 = (D_{DM} + D_{DL})K_s$

It is convenient to consider a differential mode with an assumption that load inertia is infinite and differential wheel speed $\omega_{DL} = 0$ because we can approximately represent the differential mode using much less parameters with descent agreement in case of low speed. Therefore, we can have the following block diagram (Figure 10).
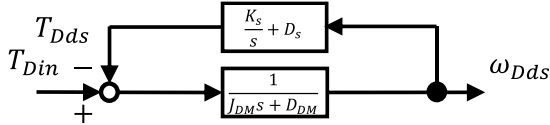

Figure 10. Block diagram of linearized TDA-TVD in differential mode with infinite load side inertia approximation.

The transfer functions of this model are given by

$$\frac{T_{Dds}}{T_{Din}} = \frac{D_s s + K_s}{J_{DL}s^2 + (D_{DM} + D_s)s + K_s} \quad (44)$$

$$\frac{\omega_{Dds}}{T_{Din}} = \frac{s}{J_{DL}s^2 + (D_{DM} + D_s)s + K_s} \quad (45)$$

Frequency Response Analysis of TDA-TVD on Differential Mode

In order to evaluate the proposed linear model of TDA-TVD on differential mode, simulations of frequency response of TDA-TVD with a simplified vehicle model were carried out. The simplified vehicle model contains a single sprung mass and four wheels with the brush model which has a nonlinear relation between the slip of the wheel and the tire force. To focus on the vibration of the driveline, suspension dynamics (vertical movement)) is neglected. The rear wheels are driven by two motors with TDA-TVD while the front wheels are not driven. The simulated vehicle has the same parameters with the experimental vehicle. Input differential torque has the amplitude of 100 Nm. Initial vehicle speed V is set to 10 m/s, which is a moderate speed as benchmark. During the simulation, steering angle is kept zero. The vehicle is assumed to be NS (i.e., $K_{DL} = 0$). The simplified nonlinear vehicle model, the obtained linear vehicle model on the differential mode and the simplified linear model with infinite load side inertia are compared together. The parameters of the simulated vehicle model and TDA-TVD are shown in Table 1.

The simulated frequency response ω_{Dds}/T_{Din} is shown in Figure 11. The proposed linear models have decent agreement with the nonlinear vehicle model above 1Hz on the gain diagram. In that case, the infinite load side inertia approximation model is enough to consider the higher frequency response. However, the infinite load side inertia approximation model has a considerable difference at the lower

frequency region. Overall, the proposed linear model on the differential mode of TDA-TVD is reasonable to emulate the real hardware.

The simulated frequency response T_{Dds}/T_{Din} is shown in Figure 12. In this figure, the realistic nonlinear model, the obtained linear model on the differential mode and the same linear model with the assumption $K_{DL} = 0, D_{DL} = D_L$. The latter linear model is convenient to design a joint torque vibration suppression controller since no parameters related to the tire are needed and therefore also compared here.

Except for the difference of the peak amplitude at the resonance frequency around 2Hz, both linear models have decent agreement with the realistic nonlinear model. Thus, the linear model with the assumption $K_{DL} = 0, D_{DL} = D_L$ is used for the controller design.

Frequency-domain System Identification of TDA-TVD on Summation-Differential Mode

An experiment of the frequency response identification of a real TDA-TVD unit was carried out. The TDA-TVD unit is connected with two individual load motor to emulate a vehicle translating and not turning, without the slip of wheels. The following parameters shown in エラー! 参照元が見つかりません。 were used to get the frequency response of the obtained summation and differential models.
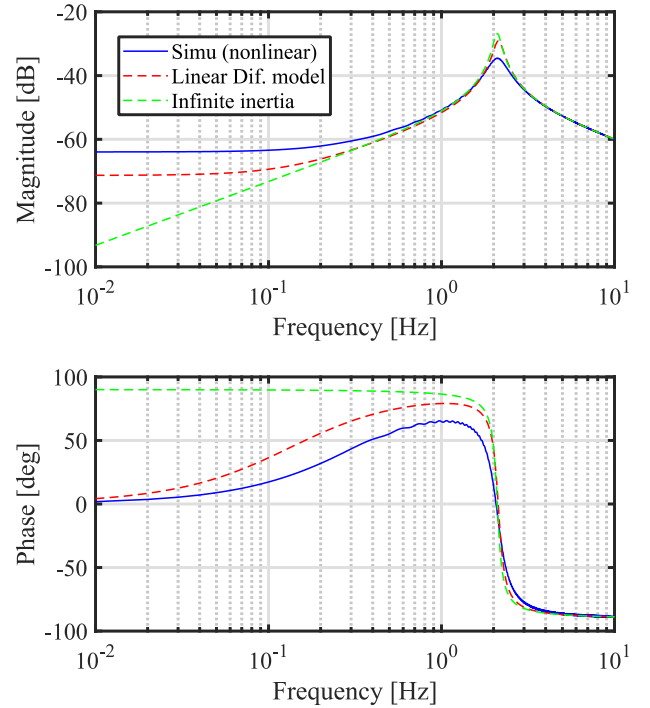

Figure 11. Bode diagram of ω_{Dds}/T_{Din} of TDA-TVD with infinite load inertia on differential mode ($V = 10$ m/s).
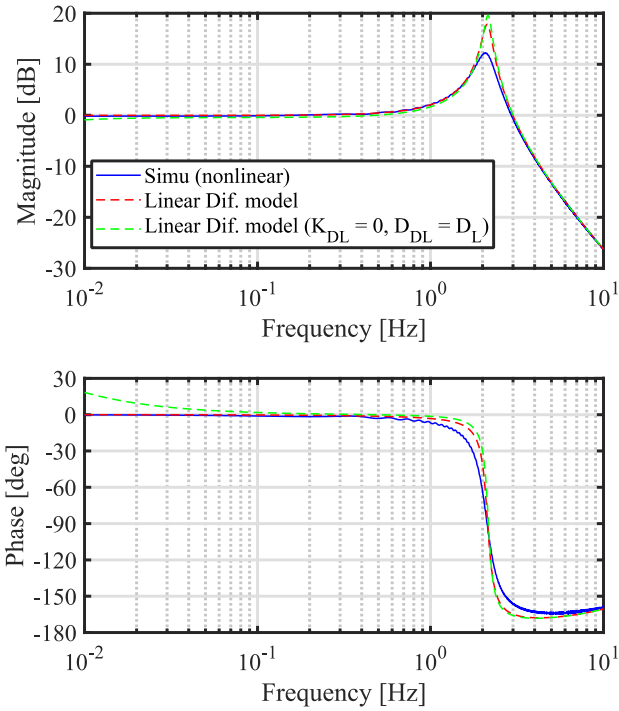
Figure 12. Bode diagram of TVD with infinite load inertia on differential mode ($V = 10$ m/s).

The experimental results of the frequency response identification are shown in Figure 13(a) and Figure 13(b). The identified frequency responses are ω_{SM}/T_{SM} and ω_{DM}/T_{DM}. In both cases, the gain and phase diagrams show certain agreement between the experimental results and obtained linear models. The phase diagrams show the discrepancy at higher frequency and this is because of the communication delay of the measured data.

Table 1. Nominal parameters of experimental vehicle with TDA-TVD unit. K_s, D_m, D_L, and D_s are identified by fitting curves (Model) of Figure 13. These parameters are also used for the simulation.

M	2173 kg
J_M, J_w, I	0.0183, 1.81, 3308 kg · m^2
K_s	2891 N/rad
D_m, D_L, D_s	0.078, 0.0625, 15 N/(rad· s)
r, d, l_f, l_r	0.338, 1.54, 1.34, 1.33 m
G, b_1, b_2	10.8, 0.892, 0.895
C_f, C_r	45495, 53438 N/rad
λ_{Dn}	0
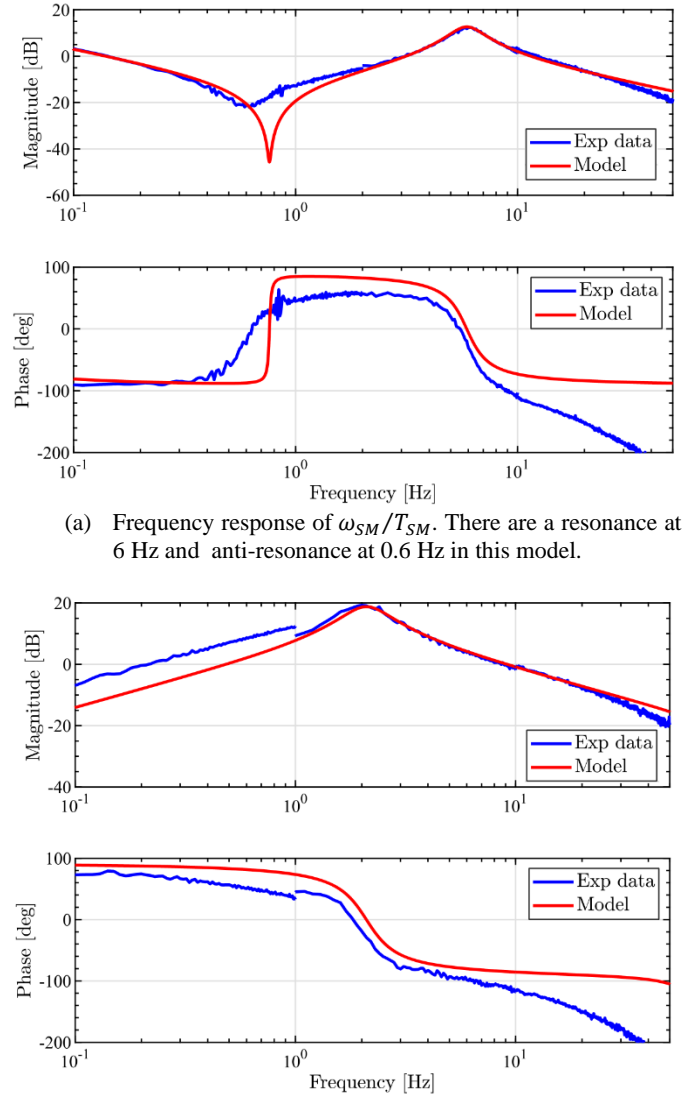
(a) Frequency response of ω_{SM}/T_{SM}. There are a resonance at 6 Hz and anti-resonance at 0.6 Hz in this model.

(b) Frequency response of ω_{DM}/T_{DM} There is a resonance at 2 Hz in this model.

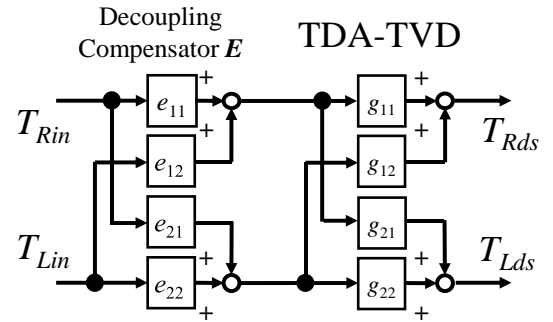Figure 13. Frequency response of TDA-TVD on summation and differential modes.

Figure 14. Decoupling compensator E is inserted before TDA-TVD.

The reason why the phase decreases at higher frequency in case of the experiments is because of sampling frequency of 100 Hz. The experiment of the system identification on differential mode was carried out on two frequency intervals from 0.01 to 1.0 Hz and 1.0 to 100 Hz separately. That is the reason that the curves of the experimental data are not continuous at 1 Hz.

SDMT enables us to construct vehicle dynamics controller much easier since we do not need to take the coupling between the left and right wheels into account. Now, two of vibration suppression controllers are proposed in this chapter.

Design of joint torque controller

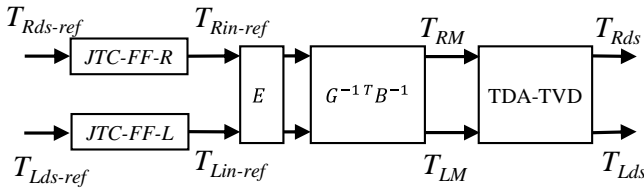### *Conventional Feedforward Controller using Decoupling Compensator*

The previous study designed a decoupling compensator E based on an "diagonalization" as shown in Figure 14 and the following parameters

$$\begin{bmatrix} e_{11} & e_{12} \\ e_{21} & e_{22} \end{bmatrix} = \begin{bmatrix} 1 & -g_{12}/g_{11} \\ -g_{21}/g_{22} & 1 \end{bmatrix} \tag{46}$$

The previous study assumed a load inertia to be that of the summation mode, i.e., $J_{RL} = J_{LL} = J_{SL}$, and $D_M = D_L = 0$. The transfer functions with the decoupling compensator E are obtained as follows

$$\begin{bmatrix} \frac{T_{Rds}}{T_{Rin}} & \frac{T_{Lds}}{T_{Rin}} \\ \frac{T_{Rds}}{T_{Lin}} & \frac{T_{Lds}}{T_{Lin}} \end{bmatrix} = \begin{bmatrix} \frac{J_{LS}(D_s s + K_s)}{J_{11}J_{LS}s^2 + D_s J_{X1}s + K_s J_{X1}} & 0 \\ 0 & \frac{J_{LS}(D_s s + K_s)}{J_{22}J_{LS}s^2 + D_s J_{X2}s + K_s J_{X2}} \end{bmatrix} \tag{47}$$

swhere $J_{X1} = J_{11} + J_{LS}$, $J_{X2} = J_{22} + J_{LS}$. The joint torque control feedforward controller with the decoupling compensator (JTC-FF-E) was constructed by the inverse of the above equations multiplied by an additional filter in the same way (see Figure 15(b)).

(a) Based on Summation-Differential mode transformation (Prop.).
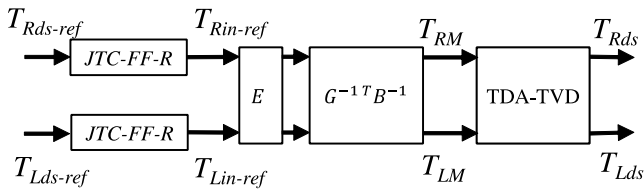
(b) Based on decoupling compensator E (Conv.).

Figure 15. Implemented block diagrams of Joint torque controllers.

Proposed Feedforward Controller using SDMT

This section designs a joint torque vibration suppression control based on SDMT. We utilize (60) and (80) to construct the feedforward of the joint torque controller based on SDMT (JTC-FF-S(D)) given by

$$C_{JTC-FF-S} = \frac{T_{Sin}}{T_{Sds}} \frac{1}{\tau s + 1} = \frac{c_3 s^3 + c_2 s^2 + c_1 s + c_0}{(J_{SL}s + D_{SL})(D_s s + K_s)(\tau s + 1)} \tag{48}$$

$$C_{JTC-FF-D} = \frac{T_{Din}}{T_{Dds}} \frac{1}{\tau s + 1} = \frac{d_3 s^3 + d_2 s^2 + d_1 s + d_0}{(J_{DL}s + D_L)(D_s s + K_s)(\tau s + 1)} \tag{49}$$

where τ is a cutoff frequency of an additional filter to make the transfer functions proper. The overall block diagram of the joint torque controller including the coordinate transformation is shown in Figure 15(a).

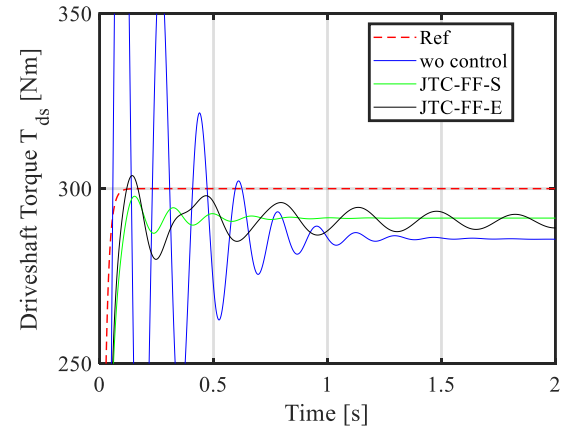### *Simulation of Joint Torque Vibration Suppression Control*

Step response simulations of the joint torque vibration suppression control are carried out in order to evaluate the performance of the controller based on SDMT. The simulated vehicle is running at 45 km/h and the driveshaft torque reference of 300 Nm for summation and differential inputs. In other words, in the case of summation inputs, $T_{Rds-ref} = T_{Lds-ref} = 300$ Nm and in the case of differential inputs, $T_{Rds-ref} = -T_{Lds-ref} = 300$ Nm.

To evaluate the effectiveness of the proposed controller, three cases are compared; without any control (wo control), JTC based on SDMT (JTC-FF-S or JTC-FF-D), and JTC based on the normal mode with the decoupling compensator (JTC-FF-E).

The simulation was carried out using MATLAB/Simulink environment. The parameters of the vehicle and TDA-TVD are the same with the previous simulations. There are no parameter differences between the actual vehicles and the controllers.
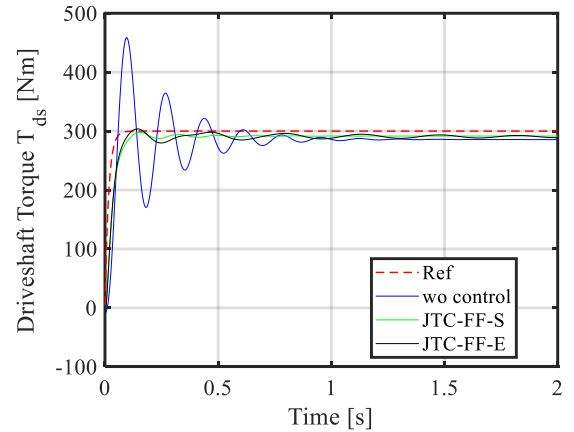
(a) Right side driveshaft torque T_{Rds} response (summation mode). Both JTC-FF

(b) Right side driveshaft torque T_{Rds} response (summation mode, zoom-in).
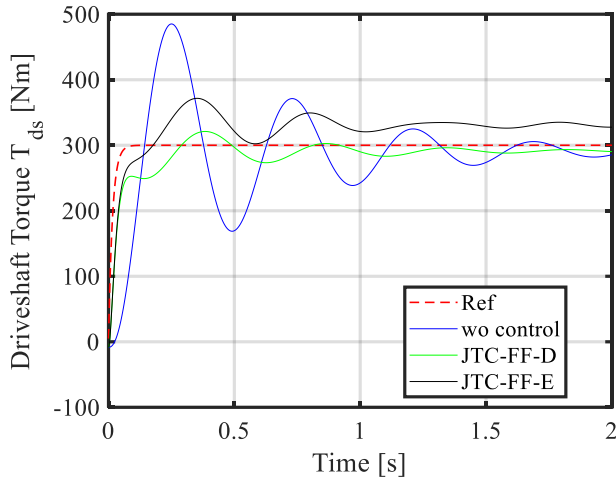
(c) Right side driveshaft torque T_{Rds} response (differential mode).

Figure 16. Simulation of joint torque vibration suppression control. SDMT based JTC (JTC-FF-D) has better tracking performance than that of based on conventional normal mode (JTC-FF-E).

Figure 16 shows simulated results on both the summation mode and differential mode. In each case, JTC based on SDMT has less vibration and less offset error compared to JTC-FF-E.

Figure 17. Experimental vehicle equipped with TDA-TVD. TDA-TVD drives rear wheels using two electric motors.

Experimental verification of joint torque vibration suppression control

In this section, an experimental verification of the joint torque vibration suppression control is carried out. To evaluate the effectiveness of the proposed controller, three cases are compared; without any control (wo control), JTC based on SDMT (JTC-FF-S or JTC-FF-D), and JTC based on the normal mode with the decoupling compensator (JTC-FF-E).

Experimental Conditions

The following two scenarios are verified on a straight dry path, and the steering angle is held at 0 degree by a driver in the whole experiment. The first scenario is that the vehicle is driven by the differential driveshaft torque reference of 450 Nm when the vehicle is running at 45 km/h. The second scenario is that the vehicle is accelerated by the summation driveshaft torque reference of 500 Nm when the vehicle is running at 20 km/h.

The experimental vehicle with TDA-TVD is shown in Figure 17. The main parameters of the vehicle are given in Table 1. TDA-TVD drives rear wheels using two electric motors. The vehicle is also equipped

with another single motor with ordinary open differential for front wheels, but they are not driven. The driving control unit uses MicroAutoBox (MAB) to output drive shaft torque command which is determined by accelerator opening degree and vehicle speed. MAB communicates with Motor Control Unit (MCU) by Controller Area Network (CAN) in a cycle of 10 ms. The controllers of JTC are implemented on the MCU. The drive shaft torque command is input to the JTC controllers through a low pass filter, whose cutoff frequency is 10 Hz. The torque command is calculated in a cycle of 1 ms. To protect TDA-TVD, the drive shaft torque command differential rate is limited by 1000 Nm/s.

Experimental Results

Fig. 18 shows the experimental results with different JTC controllers. As shown in Figure 18(a) the experimental results on differential mode, the drive shaft torque vibrates at 2 Hz when the differential torque is applied without control. It is caused by the torsional resonance of the drive shaft on the differential mode as shown in section IV. On the other hand, the vibration can be suppressed by the controller of JTC-FF-E with tuned parameters. Even though JTC-FF-D with nominal and identified parameters in Table 1 and エラー! 参照元が見つかりません。 has a constant error about 100 Nm, it could be reduced by tuning the parameters during the experiment. The controller of JTC-FF-D (tuned) obtained almost the same vibration suppression performance with JTC-FF-E (tuned).
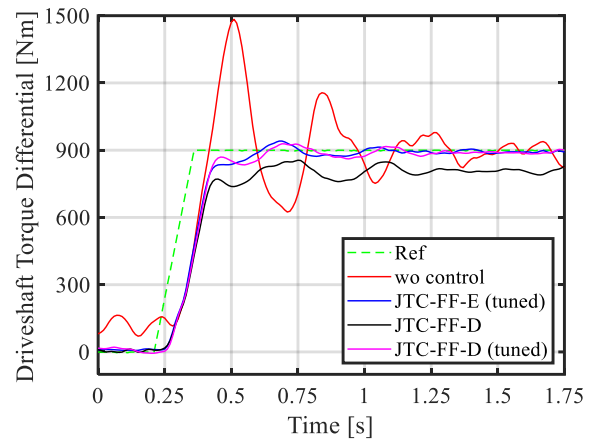
(a) Differential mode.
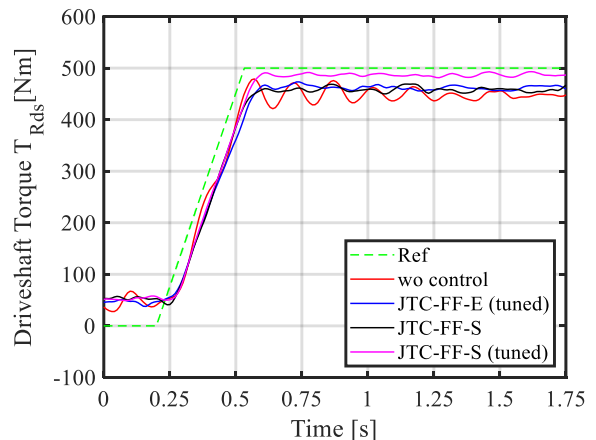
(b) Summation mode.

Figure 18. Experimental results of Joint Torque Vibration Suppression. While the proposed JTC-FF-D and the conventional JTC-FF-E equally

Figure 18(b) shows the experimental results with different JTC controllers on summation mode. The drive shaft torque vibrates at 6 Hz when the summation torque is applied. It is caused by the torsional resonance of drive shaft on summation mode. Even though the vibration can be suppressed by the controllers of JTC-FF-E with the parameters tuned in the differential experiment, there is a constant error about 30 Nm. It means that JTC-FF-E cannot handle both summation and differential modes simultaneously. On the other hand, this constant error can be reduced to about 10 Nm by tuning the parameters of JTC-FF-S. Comparing with JTC-FF-E, there is lower model error in JTC-FF-S and JTC-FF-D by tuning the parameters independently. The overall results indicate the validity of the SDMT based model and controllers effectively. The improvement of the torque control will result in better acceleration/deceleration control, yaw rate control (less deviation and vibration) and better driving stability.

Future Work

The simulations and experiments in this study assumed no discrepancies in the model parametrization. Practically, the vehicle mass M and load inertia J_L are the major parameters which can change considerably. The change of the vehicle mass could be relatively easily monitored and compensated by comparing input torques and a measured longitudinal acceleration. On the other hand, the load inertia J_L can decrease when wheels slip. To deal with this, preventing slip ratio from exceeding a certain value (e.g. 10%) by employing a traction control, or estimating slip ratio and vary the parameter of the joint torque controller accordingly, would be potential strategies.

Evaluations of drivability, ride comfort, and cornering performance (e.g., double lane change test), along with design and implementation of feedback controllers (slip ratio control, direct yaw moment control, etc.) are to be carried out in the future.

Conclusion

This study demonstrated a frequency domain analysis of TDA-TVD with a newly proposed linear model of TDA-TVD that well describes the longitudinal motion and yaw motion (summation-differential mode). The experimentally obtained frequency responses of TDA-TVD based on the summation-differential mode transformation showed descent agreement with the new model, while the responses based on a conventional normal mode did not match with a conventional model. Next, a driveshaft torque vibration suppression controller is designed based on the inverse model of the summation and differential modes. The simulation and experimental results of step torque inputs on both summation and differential modes suggested that the feedforward vibration suppression controller based on the new model has better performance in suppressing vibrations and reducing offset errors, compared to the conventional controller, which cannot the reduce offset error on the summation mode.

Design and integration of feedback controllers (such as ones seen on [27]) and further evaluations of the proposed methods on drivability, ride comfort, and cornering performance will be our future work.

References

1. Y. Shibahata, K. Shimada, and T. Tomari, "Improvement of vehicle maneuverability by direct yaw moment control", Vehicle System Dynamics, vol. 22, no. 5-6, pp. 465-481, 1993.

2. K. Sawase, Y. Ushiroda, and T. Miura, "Left-right torque vectoring technology as the core of super all wheel control (S-AWC)", Mitsubishi Motors Technology Review, vol. 18, pp. 16-23, 2006.

3. K. Sawase, "AYC + ASC", Motor Ring, Vol.7, p.18-19, 1998 (In Japanese).

4. T. Tomari, A. Mori, Y. Shibahata, "Development of SH-AWD based on DYC concept". Proceedings of AVEC'06, 0217, 2006.

5. Kakalis, L., Zorzutti, A., Cheli, F., and Travaglio, G., "Brake Based Torque Vectoring for Sport Vehicle Performance Improvement," SAE Int. J. Passeng. Cars - Mech. Syst. 1(1):514-525, 2009.

6. E. Katsuyama, M. Yamakado, and M. Abe, "A state-of-the-art review: toward a novel vehicle dynamics control concept taking the driveline of electric vehicles into account as promising control actuators," Vehicle System Dynamics, 59:7, 976-1025, 2021.

7. E. Esmailzadeh, G.R. Vossoughi and A. Goodarzi, "Dynamic Modeling and Analysis of a Four Motorized Wheels Electric Vehicle, Vehicle System Dynamics," 35:3, 163-194, 2001.

8. M. Croft-White and M. Harrison, "Study of torque vectoring for all-wheel-drive vehicles", Vehicle System Dynamics, 44:sup1, 313-320, 2006.

9. L. Zhang, H. Ding, Y. Huang, H. Chen, K. Guo and Q. Li, "An Analytical Approach to Improve Vehicle Maneuverability via Torque Vectoring Control: Theoretical Study and Experimental Validation", IEEE Trans. on Vehicular Technology, vol. 68, no. 5, pp. 4514-4526, May 2019.

10. Y. Hori, "Future vehicle driven by electricity and control research on four-wheel-motored 'UOT electric march II'", IEEE Trans. on Industrial Electronics, vol. 51, 5, pp. 954-962, 2004.

11. Y. Chen, S. Chen, Y. Zhao, Z. Gao and C. Li, "Optimized Handling Stability Control Strategy for a Four In-Wheel Motor Independent-Drive Electric Vehicle", in IEEE Access, vol. 7, pp. 17017-17032, 2019.

12. M. Chae, Y. Hyun, K. Yi and K. Nam, "Dynamic Handling Characteristics Control of an in-Wheel-Motor Driven Electric Vehicle Based on Multiple Sliding Mode Control Approach", in IEEE Access, vol. 7, pp. 132448-132458, 2019.

13. J. Zhang, W. Sun and H. Du, "Integrated Motion Control Scheme for Four-Wheel-Independent Vehicles Considering Critical Conditions", in IEEE Transactions on Vehicular Technology, vol. 68, no. 8, pp. 7488-7497, Aug. 2019.

14. Zha, Y., Quan, X., Ma, F., Liu, G. et al., "Stability Control for a Four-Wheel-Independent-Drive Electric Vehicle Based on Model Predictive Control," SAE Int. J. Veh. Dyn., Stab., and NVH 5(2):191-204, 2021.

15. R. K. Subroto, C. Z. Wang and K. L. Lian, "Four-Wheel Independent Drive Electric Vehicle Stability Control Using Novel Adaptive Sliding Mode Control," in IEEE Transactions on Industry Applications, vol. 56, no. 5, pp. 5995-6006, Sept.-Oct. 2020.

16. Y. Yang, et al, "Novel Traction Control of Electric Vehicle based on Single Wheel Dynamics", in the Journal of Engineering, vol. 2019, no.23, pp. 9006-9012, 2019.

17. D. Yin, N. Sun and J. Hu, "A Wheel Slip Control Approach Integrated With Electronic Stability Control for Decentralized Drive Electric Vehicles", in IEEE Transactions on Industrial Informatics, vol. 15, no. 4, pp. 2244-2252, April 2019.

18. J. Fengjiao, L. Zhiyuan and Z. Hongliang, "A traction control strategy based on optimal slip ratio for the in-wheel motor electric vehicle while steering", 2015 34th Chinese Control Conference (CCC), Hangzhou, pp. 8171-8176, 2015.

19. Dzmitry Savitski, Valentin Ivanov, Tomoki Emmei, Hirojuki Fuse, Hiroshi Fujimoto, and Leonid Fridman, "Wheel Slip Control for the Electric Vehicle with In-Wheel Motors: Variable Structure and Sliding Mode Methods" IEEE transaction on Industrial Electronics, vol. 67, no. 10, 8535-8544, Oct. 2019.

20. Aouadj, N., Hartani, K., and Fatiha, M., "New Integrated Vehicle Dynamics Control System Based on the Coordination of Active Front Steering, Direct Yaw Control, and Electric Differential for Improvements in Vehicle Handling and Stability," SAE Int. J. Veh. Dyn., Stab., and NVH 4(2):119-133, 2020.

21. Hu, Z., Liao, Y., Liu, J., and Xu, H., "Investigation of Vehicle Stability by Integration of Active Suspension, Torque Vectoring, and Direct Yaw Control," SAE Int. J. Veh. Dyn., Stab., and NVH 6(4):441-459, 2022.

22. Z. Li, H. Chen, H. Liu, P. Wang and X. Gong, "Integrated Longitudinal and Lateral Vehicle Stability Control for Extreme Conditions With Safety Dynamic Requirements Analysis," in IEEE Transactions on Intelligent Transportation Systems, vol. 23, no. 10, pp. 19285-19298, Oct. 2022.

23. E. Hashemi, M. Jalali, A. Khajepour, A. Kasaiezadeh and S. K. Chen, "Vehicle Stability Control: Model Predictive Approach and Combined-Slip Effect," in IEEE/ASME Transactions on Mechatronics, vol. 25, no. 6, pp. 2789-2800, Dec. 2020.

24. Li, S., Wang, G., Zhang, B. et al. "Vehicle Yaw Stability Control at the Handling Limits Based on Model Predictive Control." Int.J Automot. Technol. 21, 361–370, 2020.

25. Y. Chen, S. Chen, H. Ren, Z. Gao and Z. Liu, "Path Tracking and Handling Stability Control Strategy With Collision Avoidance for the Autonomous Vehicle Under Extreme Conditions," in IEEE Transactions on Vehicular Technology, vol. 69, no. 12, pp. 14602-14617, Dec. 2020.

26. M. Rokonuzzaman, N. Mohajer, S. Nahavandi and S. Mohamed, "Model Predictive Control With Learned Vehicle Dynamics for Autonomous Vehicle Path Tracking," in IEEE Access, vol. 9, pp. 128233-128249, 2021.

27. Sawase. K, Chiba M, "Study of Lateral Torque-vectoring Differential Suitable for Electric Powered Vehicles", Transactions of Society of Automotive Engineers of Japan, Vol.45-5, p.823-828, 2014 (In Japanese).

28. Sawase. K, et.al., "Classification and Analysis of Torque-vectoring Differentials with Torque Difference Amplification Mechanism", Transactions of Society of Automotive Engineers of Japan, Vol.48, No.2, p.317-322, 2017 (In Japanese).

29. H. Kawamura, K. Ito, T. Karikomi, and T. Kume, "Highly-Responsive Acceleration Control for the Nissan LEAF Electric Vehicle", SAE Technical Paper 2011-01-0397, 2011.

30. A. Scamarcio, M. Metzler, P. Gruber, S. De Pinto and A. Sorniotti, "Comparison of Anti-Jerk Controllers for Electric Vehicles With On-Board Motors", IEEE Transactions on Vehicular Technology, vol. 69, no. 10, pp. 10681-10699, Oct. 2020.

31. H. Sumiya and H. Fujimoto, "Driving Force Control Method Using Suppression Control of Driving-shaft Vibration for Electric Vehicle with On-board Motor", in Proc. IEEJ Industry Applications Society Conf, no. 106, 2012, pp. 115–120 (in Japanese).

32. V. Ivanov, D. Savitski, J. Orus, J. M. Rodriguez Fortun, A. Sorniotti and P. Gruber, "All-wheel-drive electric vehicle with on-board motors: Experimental validation of the motion control systems," IECON 2015 - 41st Annual Conference of the IEEE Industrial Electronics Society, Yokohama, Japan, 2015, pp. 001729-001734.

33. S. Wakui, T. Emmei, H. Fujimoto, Y. Hori, "Gear Collision Reduction of Geared In-wheel-motor by Effective Use of Load-side Encoder", The 45th Annual Conference of the IEEE Industrial Electronics Society, Lisbon, Portugal, pp.3469-3474, 2019.

34. S. Sato and H. Fujimoto, "Proposal of Pitching Control Method Based on Slip-Ratio Control for Electric Vehicle", Proc. The 34th Annual Conference of the IEEE Industrial Electronics Society, pp. 2823–2828, 2008.

35. K. Kawashima, T. Uchida, and Y. Hori, "Rolling stability control of in-wheel electric vehicle based on two-degree-of-freedom control", Proc. 10th IEEE International Workshop on Advanced Motion Control, pp.751–756, 2008.

36. H. Fukudome, "Reduction of Longitudinal Vibration Using In-Wheel Motors", Trans. JASE, Vol. 47, No. 2, pp. 457-462, 2016. (in Japanese)

37. N. Ochi, H. Fujimoto, Y. Hori, "Roll and pitch Control using Positive and Negative Anti-dive Force for Electric Vehicle with Four In-wheel Motors", in Proceedings on IEEJ Industry Applications 174 References Society Conference, Vol. 4, pp. 133-136, 2016.

38. H. Fuse, H. Fujimoto, K. Sawase, N. Takahashi, R. Takahashi, Y. Okamura, R. Koga, "Derivation of Dynamic Model of Two-Input-Two-Output Torque Difference Amplification Motor Drive System and Independent Left-and-Right Wheel Control with Decoupling Compensator", IEEJ Journal of Industry Applications, Vol. 11, No. 3, pp. 427-436, 2022.

39. W. Ohnishi, et. al, "Decoupling Control Method for High-Precision Stages using Multiple Actuators considering the Misalignment among the Actuation Point, Center of Gravity, and Center of Rotation", IEEJ Journal of Industry Applications, Vol.5, No.2, pp.141-147, 2016.

40. S. Katsura and K. Ohnishi, "Quarry of Modal Information from Environment for Advanced Motion Control", IEEJ Transactions on Industry Applications, vol. 126, no. 4, pp. 372-378, 2006.

41. M. Abe, "Vehicle handling dynamics: theory and application", Butterworth-Heinemann, 2015.

Definitions/Abbreviations

Symbol	Definition
M	Mass of vehicle (including passengers and on board loads)
I	Yaw inertia of vehicle
r	Effective radius of wheel
l_f, l_r	Distance between the front or rear axle and the longitudinal center of gravity
C_f, C_r	Cornering stiffness of front or rear wheel
d	Tread
$J_{R(L)\omega}, J_{R(L)M}, J_{R(L)L}$	Inertia of wheel, motor, and nominal load (R: right side, L: left side)
$G_{R(L)}, \boldsymbol{G}$	Primary reduction gear ratio and its formulated diagonal 2x2 matrix
b_1, b_2	Equivalent secondary reduction gear ratio
$\boldsymbol{B}$	A 2x2 matrix which represents differential torque amplitude
$\boldsymbol{P_L}, \boldsymbol{P_M}, \boldsymbol{P_{ds}}$	2x2 diagonal matrices which represent dynamic model (transfer function) of load,

		motor, and driveshaft respectively
$K_{R(L)s}$		Stiffness of driveshaft
$D_{R(L)s}$, $D_{R(L)M}$, $D_{R(L)L}$		Damping coefficient of driveshaft, motor, and wheel
$T_{R(L)M}$, $\boldsymbol{T}_M$		Input motor torque and its formulated 1x2 vector
$T_{R(L)Dm}$		Input motor torque after primary gear reduction
$T_{R(L)m}$		Transmitted motor torque to planetary gears
$T_{R(L)in}$, $\boldsymbol{T}_{in}$		Input motor torque converted to driveshaft side and its formulated 1x2 vector
$T_{R(L)ds}$, $\boldsymbol{T}_{ds}$		Driveshaft torque after secondary gear reduction and its formulated 1x2 vector
$T_{R(L)L}$, $\boldsymbol{T}_L$		Load torque and its formulated 1x2 vector
$\omega_{R(L)M}$, $\boldsymbol{\omega}_M$		Motor side angular speed before gear reduction and its formulated 1x2 vector
$\omega_{R(L)m}$, $\boldsymbol{\omega}_m$		Motor side angular speed after gear reduction and its formulated 1x2 vector
$\omega_{R(L)ds}$, $\boldsymbol{\omega}_{ds}$		Driveshaft side angular speed and its formulated 1x2 vector
$\omega_{R(L)L}$, $\boldsymbol{\omega}_L$		Wheel angular speed and its formulated 1x2 vector
V		Vehicle body speed
γ		Yaw rate
β		Sideslip angle of vehicle body
a_y		Lateral acceleration
δ_f		Steering angle
$\lambda_{R(L)}$		Slip ratio
s		Laplace transformation operator